ACS NANO

Open Access

www.acsnano.org

An Emergent Chiral Spin Crystal Phase in (111) $SrRuO_3$ Thin Films

Zhaoqing Ding, Yongjie Xie, Sheng Wang, Xuejiao Chen, Zhen Wang, Zeguo Lin, Enling Wang, Xiaofeng Wu, Mingyu Yang, Yuelong Xiong, Meng Meng, Fang Yang, Jiandi Zhang, Xianggang Qiu,* Xiaoran Liu,* and Jiandong Guo*

Cite This: *ACS Nano* 2026, 20, 603−611

Read Online

ACCESS | Metrics & More | Article Recommendations | Supporting Information

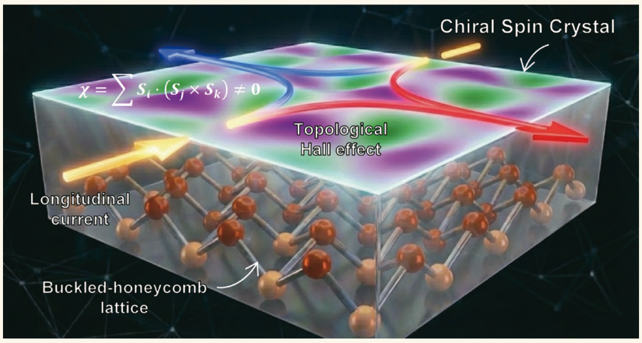

ABSTRACT: **Perovskite ruthenates are fascinating playgrounds for exploring topological spin textures but generally rely on extrinsic mechanisms to trigger the noncoplanar states. Here, we report the discovery of an emergent chiral spin crystal phase in (111) $SrRuO_3$ epitaxial films, characterized by a significant topological Hall effect and noncoplanar spin arrangements with different propagation vectors along two orthogonal directions. Instead of being driven by the enhanced Dzyaloshinskii−Moriya interaction due to broken inversion symmetry at heterointerfaces, this emergent state arises intrinsically from the interplay of dipolar interactions and magnetic frustration, leading to the stabilization of topological phases in much thicker films. These findings highlight a potential route for creating and controlling the topological spin states in perovskites with broad implications for spintronic device design.**

KEYWORDS: *chiral spin crystal, topological Hall effect, (111) strain engineering, perovskite ruthenates, magnetic frustration*

INTRODUCTION

The emergence of noncoplanar spin textures in magnetic materials often activates the chirality degrees of freedom via the adjacent three-spin scalar product, $\chi = \vec{S_i} \cdot (\vec{S_j} \times \vec{S_k})$, giving rise to fertile topologically nontrivial states.[1−5] These include the magnetic quasi-particles (e.g., skyrmions and merons) with definitive topological winding numbers and periodic noncoplanar spin textures with multiple propagation Q vectors along different directions—magnetic spin crystals.[6−12] The resultant nonzero scalar chiralities generate an additional contribution to the Hall effect through the spin Berry phase, termed as the topological Hall effect (THE), which is generally regarded as the hallmark of chiral spin states.[13−19] These fascinating quantum states of matter have been innovating the understanding of the topological and geometrical aspects of correlated systems and exhibiting potential applications in the fields of spintronics, next-generation memory devices, and quantum computing.[20−22]

Recently, the perovskite ruthenate $SrRuO_3$ has attracted significant attention for investigating topological spin states.[23−28] Bulk $SrRuO_3$ is a 4d itinerant ferromagnet below its Curie temperature (T_C) around 150 K, with a saturated magnetization of ∼1.6 μ_B per Ru^{4+} ion.[29,30] Based on numerous experimental efforts, a seemingly generic design paradigm has been established. Specifically, heterostructures composed of a (001)-oriented ultrathin $SrRuO_3$ slab of only several unit cells (u.c.) thickness and oxides with strong spin−orbit coupling or ferroelectric oxide layers were constructed to induce substantial Dzyaloshinskii−Moriya (DM) interaction at the interface, which is key to triggering noncoplanar spin textures in $SrRuO_3$. Following this strategy, magnetic skyrmion phases have been reported in $SrRuO_3/SrIrO_3$,[24] $SrRuO_3/BaTiO_3$,[25] and $SrRuO_3/BiFeO_3$[26] systems and an incommensurate spin crystal phase in the $SrRuO_3/PbTiO_3$ system.[27]

However, several limitations and issues are brought about by this paradigm. First, the DM interaction as the driving force of noncoplanar spin textures is extrinsically induced from the interface, whose decaying magnitude leads to the formation of compelling magnetic phases that are fragile and stabilized only within very few unit cells of $SrRuO_3$. In addition, for $SrRuO_3$ thin films below a thickness of ∼10 u.c. (about 4 nm), the T_C

Received: August 20, 2025
Revised: December 20, 2025
Accepted: December 22, 2025
Published: December 29, 2025

https://doi.org/10.1021/acsnano.5c14252

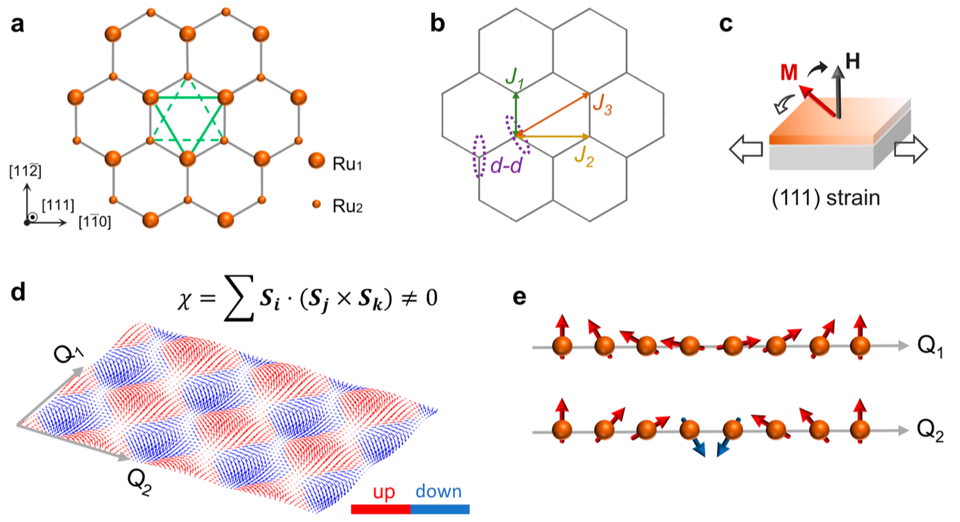

Figure 1. Schematic of the chiral spin crystal phase. (a) The buckled honeycomb lattice constructed by two neighboring Ru layers of $SrRuO_3$ along the [111] direction. Ru_1 and Ru_2 refer to the Ru atoms of respective layers. (b) The dipolar interaction and the nearest-neighbor interactions up to the third order. (c) Illustration of the competition between Zeeman energy and tensile-strain-induced magnetic anisotropy. (d) Overview of the double-Q chiral spin crystal phase on the buckled honeycomb lattice. (e) Schematics of the cycloidal spin arrangements along two orthogonal Q_1 and Q_2 directions.

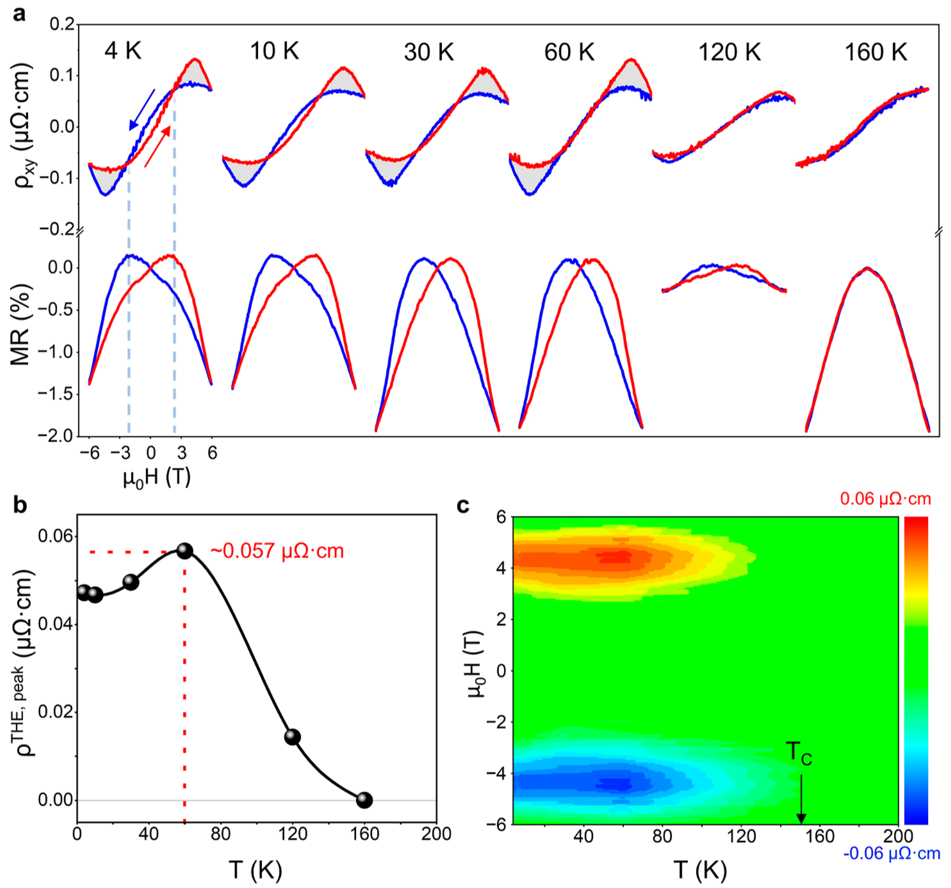

Figure 2. THE in (111) $SrRuO_3$ thin films. (a) The Hall resistivity ρ_{xy} and the longitudinal magnetoresistance MR at different temperatures across T_C. The blue curves refer to scans recorded by sweeping the magnetic field from positive to negative, whereas the red ones from negative to positive. The hump-like THE contribution at each temperature is shadowed in gray. (b) The peak value of THE as a function of temperature. (c) Mapping of the extracted topological Hall resistivity as a function of temperature and magnetic field.

drops rapidly until the complete suppression of ferromagnetism near the two-dimensional limit. As a result, the associated topologically nontrivial spin states also emerge at rather low temperatures.[23−28] On the other hand, it also calls into question the topological interpretation of the THE observed in ultrathin $SrRuO_3$ slabs because inhomogeneous issues caused by defects,[31,32] thickness variation,[33−35] or structural modification at the interfaces[36] are inevitably magnified, such that

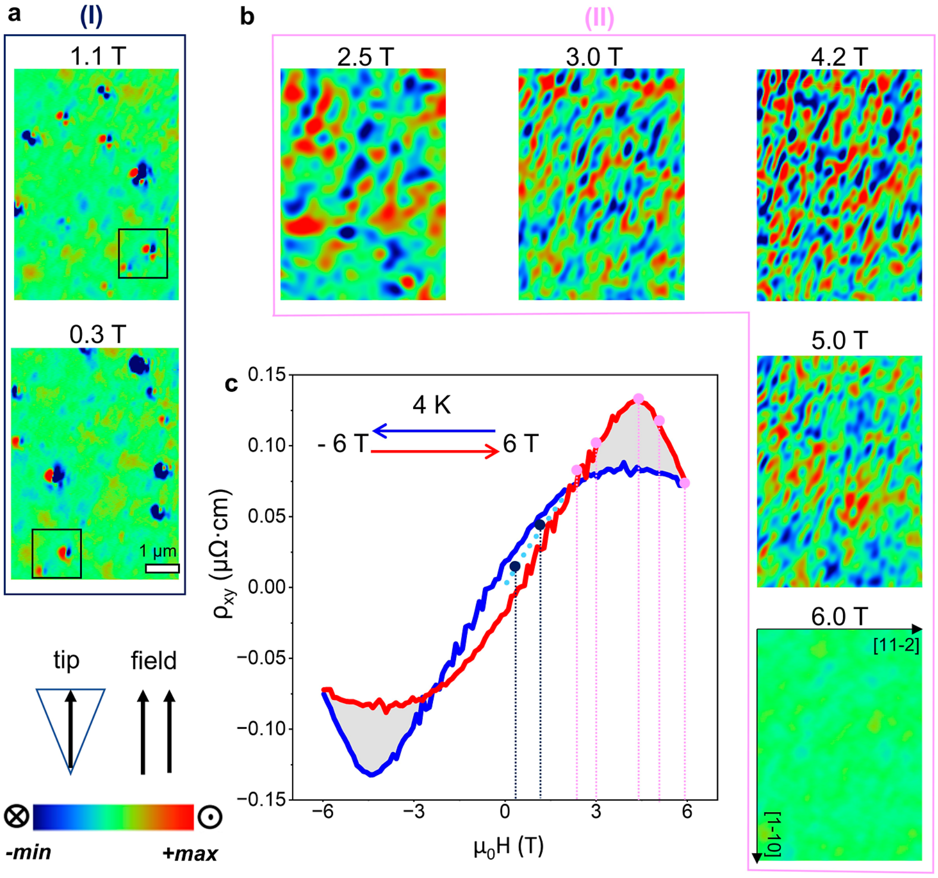

Figure 3. Evolution of magnetic domains in (111) $SrRuO_3$ thin films at 4 K. (a) MFM images recorded in regime (I) at 0.3 and 1.1 T on the initial magnetization process. The color bars stand for a frequency range from −1.0 to 1.0 Hz, covering a total scanning area of 5 × 7 μm. The outlined area on each figure in the black box highlights the splitting of the magnetic bubbles. (b) MFM images recorded in regime (II) at a set of magnetic fields on the hysteretic branch with a backward sweeping direction. The color bars stand for a frequency range from −0.35 to 0.35 Hz. The crystallographic [1−10] and [11−2] directions are marked on the image of 6 T. (c) The full hysteresis loop of Hall resistivity at 4 K. The dark blue and pink circles refer to where the MFM scans were recorded in regimes (I) and (II), respectively.

the topological Hall signal may be alternatively interpreted as a summation of multiple anomalous Hall signals resulting from different types of inhomogeneity.[37] All these highlight the need for a more intrinsic paradigm to develop robust topological spin states in $SrRuO_3$.

While the honeycomb-related lattices being the heart of exploring topological electronic states,[38−44] it has been lately recognized as a promising playground for topological spin states as well, since the coupled spin and charge degrees of freedom of electrons can lead to strong frustration due to the competition among anisotropic exchange interactions and multiple−spin interactions.[11] Notably, honeycomb-like lattice motifs are naturally established by stacking a perovskite along the [111] direction (e.g., when viewed along the [111] direction of $SrRuO_3$, two neighboring Ru atomic planes set in a buckled honeycomb lattice [Figure 1a,b]).

In this Letter, we report on the experimental realization of a chiral spin crystal phase in (111)-oriented $SrRuO_3$ epitaxial thin films [Figure 1c−e]. Remarkable and robust THE was observed right below the Curie temperature at 152 K, within a magnetic field range of 2.5−6 T. Concurrently with the THE, magnetic force microscopy (MFM) imaging provided direct real-space evidence on the formation of periodic noncoplanar spin textures with propagation vectors along two directions, denoted as the “double-Q” chiral spin crystal. The exotic spin structures can be reasonably described as a superposition of two orthogonal cycloidal spin spirals. Theoretical micromagnetic simulations corroborate that the driving force is not from DM interaction associated with interfacial broken inversion symmetry but from frustrated interactions given by the (111) lattice geometry and reveal the essence of dipolar interaction and higher-order anisotropic interactions as decisive parameters to this emergent spin state.

RESULTS AND DISCUSSION

Magnetic Chiral Spin Crystal. Epitaxial (111) $SrRuO_3$ thin films (∼20 nm) were fabricated using the pulsed laser deposition technique on $TbScO_3$ substrates. Structural characterizations demonstrate the high crystallinity of films with a coherent strain status. Notably, previous studies have revealed a tendency of (111) $SrRuO_3$ epitaxial films toward the easy-in-plane magnetic anisotropy as the magnitude of tensile strain reaches +1.5% on the $KTaO_3$ substrate.[45,46] Here, $TbScO_3$ provides a moderate tensile strain of +0.5%; this specific magnitude of tensile strain is the decisive factor. It breaks the cubic symmetry, tilting the magnetic easy axis approximately ∼75° away from the film normal and projected along the [−101] direction in the (111) plane. Tian et al. employed density functional theory calculations to investigate epitaxial strain-induced modifications in $SrRuO_3$, yielding consistent results.[47] The temperature dependence of resistivity $\rho(T)$ indicates a metallic behavior for the entire measured

https://doi.org/10.1021/acsnano.5c14252

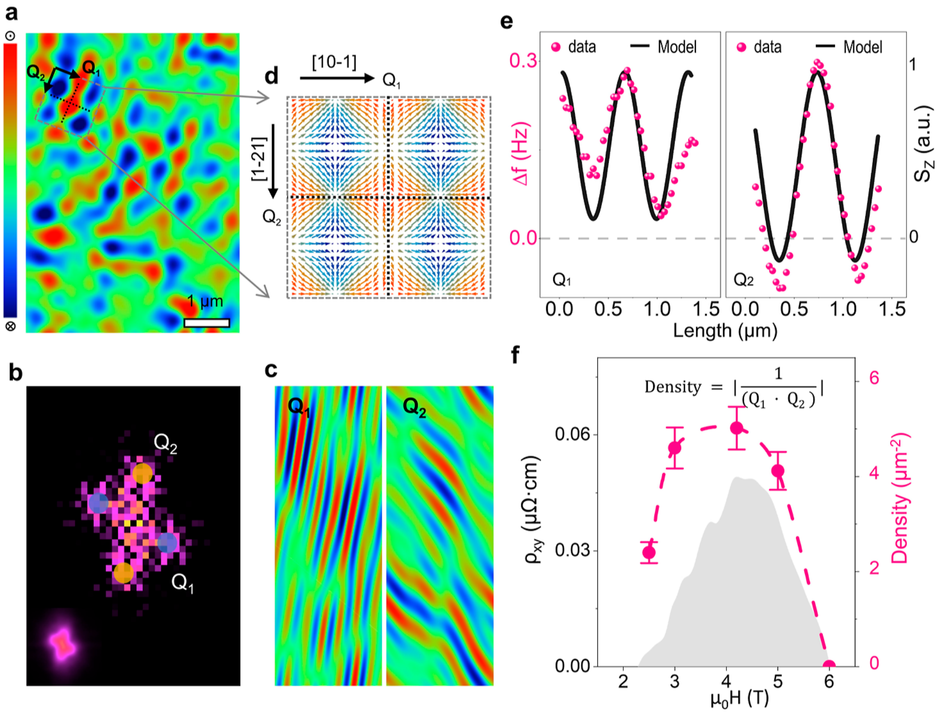

Figure 4. Fourier analyses and model illustration of the double-Q chiral spin crystal phase. (a) The 2.5 T MFM image after noise filter. (b) Emergence of the double-Q feature at 2.5 T on the FFT image, with the overall appearance shown at the left corner. (c) Isolated MFM images along each Q direction by inverse FFT. (d) Simulated spin arrangements as a superposition of two orthogonal cycloidal spin spirals, projected along the out-of-plane direction. The propagation vectors Q_1 and Q_2 are approximately aligned along the crystallographic [10−1] and [1−21] directions, respectively. (e) MFM data extracted from the line scans marked on (a) and the corresponding spin z component from the line cuts on (d). (f) Plot of the Hall resistivity ρ_{xy} and the density of the double-Q spin crystal as a function of magnetic field at 4 K.

temperature range with a 'kink' near 152 K, referring to the para-to-ferromagnetic transition [see Figure S1 for more details].

The Topological Hall Effect in (111) $SrRuO_3$. We first discuss the THE results. Figure 2a exhibits the Hall resistivity ρ_{xy} and the magnetoresistance (MR) measured at a set of temperatures across the Curie point. At T = 160 K above T_C, neither ρ_{xy} nor MR shows hysteresis. In contrast, hysteretic MR and remarkable THE signals are clearly captured below T_C, manifested as the hump-like features shaded in gray on each ρ_{xy} curve. Before regarding THE as an indication of chiral spin textures, we rule out the possibility that the observed hump-like feature is originated from the summation of two opposite AHE signals for the following important factors: (1) The THE caused by two AHEs is often present at rather low temperatures and the overall line shapes are highly sensitive to the magnetic field,[35,48] whereas the THE of our (111) $SrRuO_3$ thin films is robust. (2) If the two-AHE scenario should be present, it would produce steps on the MR curves,[49,50] which are absent in our case. (3) Our films are about 20 nm (corresponding to 87 u.c. along (111) orientation), such that the inhomogeneous issues induced by thickness or defects are practically negligible.[37] This is further corroborated by comparison to the behaviors of (111) $SrRuO_3$ films of the same thickness on $SrTiO_3$ substrates, where clean and conventional AHE signals are observed without any THE signature [Figure S16].

To make a quantitative estimate, we extract the THE contribution ρ_{THE} by taking the difference in ρ_{xy} between upward and downward field scans.[19,50,51] As shown in Figure 2b, the peak value of the THE humps ($\rho_{THE,\ peak}$) increases rapidly below the Curie temperature, reaching a maximum of ∼0.057 μΩ·cm near 60 K, and tends to level off to ∼0.05 μΩ·cm at the base temperature. Such a nonmonotonic variation of ρ_{THE} as a function of temperature is consistent with the THE behaviors reported in other systems such as $CrTe/SrTiO_3$,[52] MnSi,[53] and $Tm_3Fe_5O_{12}$/Pt.[54] Mapping of the ρ_{THE} intensity versus field and temperature further demonstrates that the THE signals are markedly observed below T_C within a field range of 2.5−5.5 T [Figure 2c]. Considering the much narrower loop of magnetization with a coercivity of ∼0.6 T [Figures S10 and S11], the presence of THE therefore plausibly signifies the formation of chiral spin states.

Evolution of the Magnetic Structure in (111) $SrRuO_3$ Thin Films. Next, we perform MFM imaging at low temperatures to provide real-space insights[55−57] into the magnetic structures and shed light on the evolution of domains [Figure 3a,b]. In particular, in order to set up a comprehensive correspondence to the THE, the MFM images were recorded at a set of field spots in two regimes covering the entire ρ_{xy} loop, as marked in Figure 3c. In regime (I) on the initial magnetization curve, there are magnetic bubble-like features observed at 0.3 and 1.1 T, which are randomly distributed on top of the overall weak contrast. Strikingly, the bubbles always appear in pairs with opposite out-of-plane magnetization components, which can be further split as the field increases. In regime (II) on the THE hysteretic branch, however, stripe-like domains with interpenetrated opposite components appear at 2.5 T, which are more prominently seen at 3.0 and 4.2 T for sharper contrast and become faded at 5.0 T. Eventually, at 6.0 T, the stripe domains diminish and the film is fully polarized into a single domain. It is noteworthy that the MFM

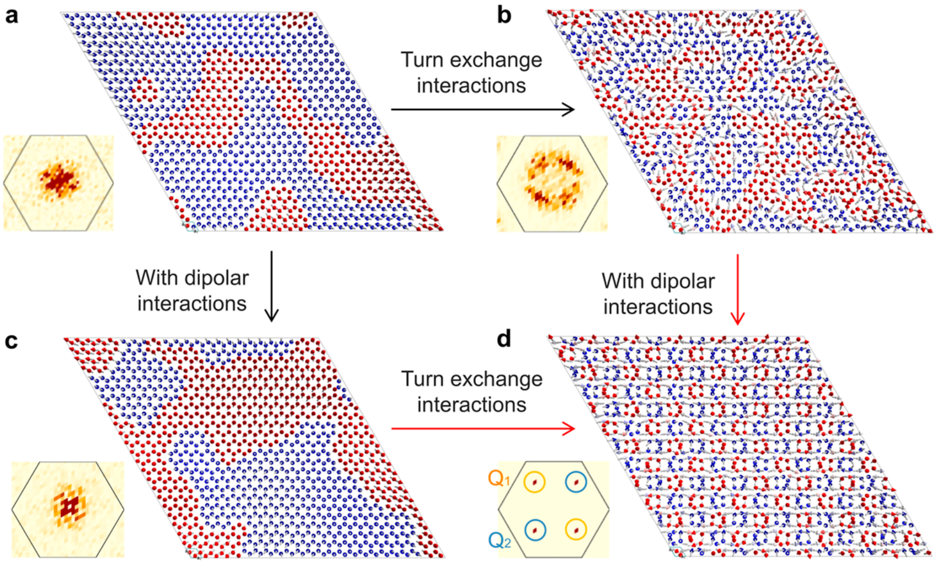

Figure 5. Monte Carlo micromagnetic simulations on the buckled honeycomb lattice. The simulated spin structures are obtained in the cases of (a) no dipolar interactions and bulk-like parameters; (b) no dipolar interactions and manipulated exchange interactions; (c) with dipolar interactions and bulk-like parameters; and (d) with dipolar interactions and manipulated exchange interactions. The corresponding FFT images in each case are displayed at the bottom.

experiments were also conducted at 10 K [Figure S5], giving rise to similar observations. Combined with the robust THE observed in Figure 2, this confirms that the stripe-like domains constitute a reproducible steady state within its phase window, maintaining stability throughout thermal-field cycling. These results therefore unravel the significant difference in domain characteristics, indicating a fundamental distinction between the presence and absence of THE in our (111) $SrRuO_3$ films.

Model Analysis of the Double-*Q* Noncoplanar Magnetic Structure. More information about the domain characteristics is obtained from fast Fourier transform (FFT) analyses of the MFM images. While the FFT images in regime (I) are overall isotropic with one central peak, anisotropic patterns with two pairs of peaks emerge at 2.5 T, labeled as Q_1 and Q_2, as shown in Figure 4b, corresponding to real-space periodicities of ~671 ± 45 nm and ~622 ± 38 nm along the [10−1] and [1−21] directions, respectively. This leads to a periodic spin superstructure embedded on the lattice, termed a spin crystal phase. The isolated MFM images for each Q vector obtained from inverse FFT clearly demonstrate that the stripe-like domains are indeed manifested as the periodic modulations of the out-of-plane magnetization along two directions [Figure 4c]. Although two period modulations exhibit short-range distortions in amplitude and orientation domains, long-range magnetic order maintains [Figure 4b]; these variations are caused by region-specific magnetic pinning effects. Notably, the "double-*Q*" feature is concomitant to the THE, which persists to 5.0 T with varying magnitudes of the Q vectors and finally vanishes at 6.0 T, when a saturated ferromagnetic domain is established [Figure S7].

The noncoplanar spin configurations of the spin crystal phase can be reasonably simulated as a superposition of two orthogonal cycloidal spin spirals.[58] Specifically, the normalized local spin vector $S(x, y)$ is expressed as

$$S(x, y) = I(x, y)[(\sin(Q_y y), 0, \cos(Q_y y)) + (0, \cos(Q_x x), \sin(Q_x x))]$$

$$I(x, y) = \frac{1}{\sqrt{(\sin(Q_y y))^2 + (\cos(Q_x x))^2 + (\cos(Q_y y) + \sin(Q_x x))^2}} \quad (1)$$

where $I(x, y)$ is the normalization factor to ensure all spins of the same magnitude. Q_x and Q_y refer to the propagation vectors along the x and y directions, respectively, whose values are determined by the FFT analyses. The resultant spin configurations projected along the z direction are exhibited in Figure 4d. The variations of the MFM data extracted from the two orthogonal line scans drawn in Figure 4a are in accord with those from the simulated magnitudes of the spin z-component, as shown in Figure 4e.

It should be clarified that the spins do not form a perfect skyrmion crystal, as skyrmions require the full wrapping of magnetization onto a unit sphere, leading to the out-of-plane magnetization reversed completely at the center with respect to the boundary.[1,59,60] Nevertheless, in analogy to the relationship between skyrmions and the THE, where the Hall resistivity is proportional to the number of skyrmions ($\rho_{THE} \propto n_{sk}$),[61] the spin crystal phase also exhibits similar correspondence (i.e., $\rho_{THE} \propto D$, D is the density of the noncoplanar spin textures, defined as $D = |1/(Q_1 \cdot Q_2)|$). This is visualized in Figure 4f by the simultaneously increasing and decreasing of ρ_{xy} and D as a function of magnetic field, suggesting the spin crystal phase with nonzero chiralities, giving rise to contributions to THE via the spin Berry phase. Notably, Q_1 remains nearly constant within experimental uncertainty, whereas Q_2 decreases with increasing magnetic field [Table S1]. This distinct behavior likely arises from their differing magnetic anisotropy directions relative to the propagation vectors under a [111]-oriented field. For Q_1 (along [10−1]), the easy-axis anisotropy pins spin orientations, generating a strong restoring force that stabilizes its wavelength against field variations. In contrast, Q_2 (along [1−21]) lies perpendicular to the easy axis, where weaker anisotropy competes with the Zeeman energy, resulting in a field-dependent wavelength reduction.

Monte Carlo Micromagnetic Simulations. Now, we discuss the possible mechanism for the emergent chiral spin crystal phase in our (111) $SrRuO_3$ thin films. The formation of noncoplanar spin textures usually requires the presence of strong DM interaction, or dipolar interactions, and/or frustration induced by multiple magnetic interactions.[6−9,12] Seddon et al. lately reported a similar incommensurate spin crystal phase in (001) $SrRuO_3/PbTiO_3$ bilayers, where the interfacial DM interaction significantly enhanced by the ferroelectric $PbTiO_3$ layer plays the decisive role in stabilizing the noncoplanar spin textures in a 6 u.c. ultrathin $SrRuO_3$ layer.[27] However, the interfacial DM interaction is unlikely the dominant factor in our case, due to the absence of any ferroelectric layer plus the much larger thickness of the films (~20 nm).[62] Alternatively, stabilization of the chiral spin crystal phase plausibly can rely on the presence of dipolar interactions and the delicate balance among multiple magnetic interactions.[62−66]

To further examine this mechanism and pinpoint the critical parameters, Monte Carlo micromagnetic simulations[67] were conducted on a buckled honeycomb lattice using the following Hamiltonian:[68]

$$\mathbf{H} = \sum_{\langle i<j\rangle} (J_1\mathbf{S}_i\cdot\mathbf{S}_j + \lambda_1 S_i^z S_j^z) + \sum_{\langle\langle i<j\rangle\rangle} (J_2\mathbf{S}_i\cdot\mathbf{S}_j + \lambda_2 S_i^z S_j^z) + \sum_{\langle\langle\langle i<j\rangle\rangle\rangle} (J_3\mathbf{S}_i\cdot\mathbf{S}_j + \lambda_3 S_i^z S_j^z) + \sum_i A(S_i^z)^2 + E^{\mathrm{D-D}} + \sum_i \mathbf{B}\cdot\mathbf{S_i} \tag{2}$$

Here, the parameters J_n and λ_n ($n = 1, 2, 3$) denote the magnitudes of the n-order nearest-neighbor isotropic and anisotropic exchange interactions, respectively; A is the strength of the single-ion anisotropy; and $E^{\mathrm{D-D}}$ represents the dipole−dipole interactions between Ru ions. The effect of strain is equivalently included in these parameters. The calculations were run with sufficiently long steps until complete convergence of energy.

It turns out that the formation of a periodic double-Q noncoplanar spin state necessitates the presence of both dipolar interactions and manipulated exchange interactions.[69,70] Figure 5a shows the simulated spin structures in the absence of dipolar interactions, using the values of magnetic interactions (i.e., J_n, λ_n, and A) from bulk $SrRuO_3$. This gives rise to typical ferromagnetic domain features and a central peak in its FFT image, testifying the validity of the model. Then, we start exploring pathways to reach the spin crystal phase. On one hand, by tuning the exchange interactions, Figure 5b reveals the breakdown of large-scale ferromagnetic domains, replaced by short-range noncoplanar spin structures. However, no long-range superstructures with well-defined periodicities can be achieved at this stage. When the dipolar interactions are taken into account, the magnetic structure starts to exhibit periodic variations, eventually forming a periodic double-Q noncoplanar spin state, as shown in the FFT image of Figure 5d. On the other hand, if maintaining the bulk parameters and only adding the dipolar interactions, it is yet not possible to reach the spin crystal phase, as illustrated in Figure 5c, where the overall ferromagnetic domain features do not change much. In particular, establishment of the final double-Q feature requires a flip of sign of the second-order exchange anisotropy λ_2 [Table S4]. The parameter variation primarily originates from the +0.5% tensile strain, where cooperative oxygen octahedral rotations simultaneously regulate p−d orbital overlap, thereby modulating the delicate competition between the nearest-neighbor ferromagnetic exchange (J_1) and the longer-range frustration-inducing interactions (J_2, J_3). While the sign inversion of the λ_2 anisotropy term arises from trigonal distortion, this symmetry breaking naturally necessitates a reconfiguration of the magnetocrystalline anisotropy tensor; it provides specific and testable predictions for the theory.

These findings highlight the physical origin of the "double-Q" chiral spin crystal phase. The parent ferromagnetic state remains robust, necessitating enhanced frustration in accessing a new energy minimum. This strain-modified frustration originates from two mechanisms: (i) dipolar interactions counteracting easy-axis anisotropy and (ii) the reversal of λ_2, which destabilizes ferromagnetic correlations. The cooperative interplay of these effects along with the Zeeman energy drives the system from the ferromagnetic metastable state into the double-Q phase.

Conclusion. In summary, we have achieved a robust chiral spin crystal phase in $SrRuO_3$ (111) epitaxial films, characterized by periodic noncoplanar spin arrangements along two orthogonal directions and robust THE. Micromagnetic simulations suggest its origin from the interplay of dipolar interactions and magnetic frustration, without the need of constructing substantial DM interactions via a heterointerface. Our findings thus present a potential route to realizing and manipulating the topological magnetic states in $SrRuO_3$ and offer a promising platform for designing perovskite-based spintronic devices.

EXPERIMENTAL SECTION

Sample Fabrication. The (111)-oriented $SrRuO_3$ thin films were grown on 5 × 5 mm^2 $(111)_{pc}$ $TbScO_3$ single crystalline substrates by pulsed laser deposition. The $SrRuO_3$ ceramic target was ablated using a KrF excimer laser ($\lambda = 248$ nm, energy density ~2 J/cm^2) with a repetition rate of 2 Hz. The deposition was carried out at a substrate temperature of 800 °C under an oxygen atmosphere of 75 mTorr. The films were post-annealed at the growth condition for 15 min and then cooled to room temperature. A high-quality crystalline and single-phase (111) $SrRuO_3$ thin film was eventually achieved. The whole deposition process was in situ monitored by reflective high-energy electron diffraction. The synthesis of the (111) $SrRuO_3$ thin film on $SrTiO_3$ differs slightly from that on $TbScO_3$, requiring a growth temperature of 850 °C while maintaining an oxygen pressure of 75 mTorr.

Magnetic Force Microscopy. MFM measurements were performed with an Attocube-LT-SPM system with Liquid 2000 in the frequency modulation mode (FM-MFM) at $T = 10$ and 4 K. The samples were mounted on a sample holder within a chamber maintained at a high-purity helium gas with a pressure of approximately 4000 Pa. Ultrasharp tips (Nanosensor SSS-MFMR) with a tip remnant magnetization of 80 emu/cm^3 and an elastic constant of 3.0 N/m were used at a resonant frequency of 70 kHz and a relatively high tip coercivity of 125 Oe. Before the MFM measurements, the probe was saturated by using a permanent magnet for reliable and consistent MFM scans, enabling accurate investigations of the magnetic properties of the samples in our study. During the scans in the FM-MFM mode, the tip was lifted at a constant height of 60 nm above the sample surface, and the resonant frequency shift Δf proportional to the magnetic force has been recorded as a function of position. At a fixed temperature, following a 6 T field-cooling process with the magnetic field applied perpendicular to the film plane, MFM images were systematically acquired at selected field points along the ascending branch of the hysteresis loop. To ensure a comprehensive representation of the magnetization history, additional MFM imaging was conducted after zero-field cooling with data collected at two distinct field points along the initial magnetization curve.

Transport Measurements. The electrical transport measurements were performed in a Physical Property Measurement System (PPMS, Quantum Design) using the 4-point contact method. During the magneto-transport experiments, the magnetic field was applied along the [111] direction, and the current was driven along the $[1\bar{1}0]$ direction. At each temperature, the longitudinal and transverse resistances were recorded while sweeping the field in a cycle from +6 T to −6 T to +6 T. Standard symmetrization (anti-symmetrization) treatment was further applied using these two branches of data on the longitudinal (transverse) resistance to achieve pure signals of the magnetoresistance (Hall resistance).

Monte Carlo Micromagnetic Simulations. The Monte Carlo micromagnetic simulations were conducted using Sunny,[67] an open-source Julia library that implements SU(N) spin dynamics for modeling atomic-scale magnetism. Details about the models, parameters, and fitting process are shown in Section SII.

ASSOCIATED CONTENT

Supporting Information

The Supporting Information is available free of charge at https://pubs.acs.org/doi/10.1021/acsnano.5c14252.

> Structural, transport, and magnetic properties; Monte Carlo micromagnetic simulations; and auxiliary experiments: $SrRuO_3$ on $SrTiO_3$ (111) (PDF)

AUTHOR INFORMATION

Corresponding Authors

Xianggang Qiu − *Beijing National Laboratory for Condensed Matter Physics and Institute of Physics, Chinese Academy of Sciences, Beijing 100190, China; School of Physical Sciences, University of Chinese Academy of Sciences, Beijing 100049, China*; Email: xgqiu@iphy.ac.cn

Xiaoran Liu − *Beijing National Laboratory for Condensed Matter Physics and Institute of Physics, Chinese Academy of Sciences, Beijing 100190, China; School of Physical Sciences, University of Chinese Academy of Sciences, Beijing 100049, China*; orcid.org/0000-0003-0938-6109; Email: xiaoran.liu@iphy.ac.cn

Jiandong Guo − *Beijing National Laboratory for Condensed Matter Physics and Institute of Physics, Chinese Academy of Sciences, Beijing 100190, China; School of Physical Sciences, University of Chinese Academy of Sciences, Beijing 100049, China*; orcid.org/0000-0002-7893-022X; Email: jdguo@iphy.ac.cn

Authors

Zhaoqing Ding − *Beijing National Laboratory for Condensed Matter Physics and Institute of Physics, Chinese Academy of Sciences, Beijing 100190, China; School of Physical Sciences, University of Chinese Academy of Sciences, Beijing 100049, China*

Yongjie Xie − *Beijing National Laboratory for Condensed Matter Physics and Institute of Physics, Chinese Academy of Sciences, Beijing 100190, China; School of Physical Sciences, University of Chinese Academy of Sciences, Beijing 100049, China*

Sheng Wang − *Beijing National Laboratory for Condensed Matter Physics and Institute of Physics, Chinese Academy of Sciences, Beijing 100190, China; School of Physical Sciences, University of Chinese Academy of Sciences, Beijing 100049, China*

Xuejiao Chen − *School of Photoelectric Engineering, Changzhou Institute of Technology, Changzhou, Jiangsu 213002, China*

Zhen Wang − *Beijing National Laboratory for Condensed Matter Physics and Institute of Physics, Chinese Academy of Sciences, Beijing 100190, China; School of Physical Sciences, University of Chinese Academy of Sciences, Beijing 100049, China; Institute of High Energy Physics, Chinese Academy of Sciences, Beijing 100049, China*

Zeguo Lin − *Beijing National Laboratory for Condensed Matter Physics and Institute of Physics, Chinese Academy of Sciences, Beijing 100190, China; School of Physical Sciences, University of Chinese Academy of Sciences, Beijing 100049, China*; orcid.org/0009-0001-2678-8735

Enling Wang − *Beijing National Laboratory for Condensed Matter Physics and Institute of Physics, Chinese Academy of Sciences, Beijing 100190, China; School of Physical Sciences, University of Chinese Academy of Sciences, Beijing 100049, China*

Xiaofeng Wu − *Beijing National Laboratory for Condensed Matter Physics and Institute of Physics, Chinese Academy of Sciences, Beijing 100190, China; School of Physical Sciences, University of Chinese Academy of Sciences, Beijing 100049, China*

Mingyu Yang − *Beijing National Laboratory for Condensed Matter Physics and Institute of Physics, Chinese Academy of Sciences, Beijing 100190, China; School of Physical Sciences, University of Chinese Academy of Sciences, Beijing 100049, China*

Yuelong Xiong − *Beijing National Laboratory for Condensed Matter Physics and Institute of Physics, Chinese Academy of Sciences, Beijing 100190, China; School of Physical Sciences, University of Chinese Academy of Sciences, Beijing 100049, China*

Meng Meng − *Beijing National Laboratory for Condensed Matter Physics and Institute of Physics, Chinese Academy of Sciences, Beijing 100190, China*; orcid.org/0000-0003-3056-8257

Fang Yang − *Beijing National Laboratory for Condensed Matter Physics and Institute of Physics, Chinese Academy of Sciences, Beijing 100190, China*; orcid.org/0000-0003-4855-585X

Jiandi Zhang − *Beijing National Laboratory for Condensed Matter Physics and Institute of Physics, Chinese Academy of Sciences, Beijing 100190, China; School of Physical Sciences, University of Chinese Academy of Sciences, Beijing 100049, China*

Complete contact information is available at: https://pubs.acs.org/10.1021/acsnano.5c14252

Notes

The authors declare no competing financial interest.

ACKNOWLEDGMENTS

The authors deeply acknowledge A. Wu, H. Zhang, and L. Si for numerous insightful discussions and the staff from the BL07U beamline of the Shanghai Synchrotron Radiation

Facility (SSRF) for assistance on X-ray absorption spectroscopy data collection. This work is supported by the National Key R&D Program of China (Nos. 2022YFA1403000 and 2022YFA1403902) and the National Natural Science Foundation of China (Nos. 12204521, 12250710675, and 12374155, 12434007, U23A20366). A portion of this work was carried out at the Synergetic Extreme Condition User Facility (SECUF). A portion of this work was based on the data obtained at the beamline 1W1A of the Beijing Synchrotron Radiation Facility (BSRF-1W1A).

REFERENCES

(1) Tokura, Y.; Kanazawa, N. Magnetic Skyrmion Materials. *Chem. Rev.* **2021**, *121*, 2857−2897.

(2) Kurumaji, T.; Nakajima, T.; Hirschberger, M.; Kikkawa, A.; Yamasaki, Y.; Sagayama, H.; Nakao, H.; Taguchi, Y.; Arima, T.-h.; Tokura, Y. Skyrmion Lattice with a Giant Topological Hall Effect in a Frustrated Triangular-Lattice Magnet. *Science* **2019**, *365*, 914−918.

(3) Simonet, V.; Loire, M.; Ballou, R. Magnetic chirality as probed by neutron scattering. *Eur. Phys. J. Spec. Top.* **2012**, *213*, 5−36.

(4) Wen, X. G.; Wilczek, F.; Zee, A. Chiral spin states and superconductivity. *Phys. Rev. B* **1989**, *39*, 11413−11423.

(5) Okubo, T.; Chung, S.; Kawamura, H. Multiple-q states and the Skyrmion lattice of the triangular-lattice Heisenberg antiferromagnet under magnetic fields. *Phys. Rev. Lett.* **2012**, *108*, 017206.

(6) Rössler, U. K.; Bogdanov, A. N.; Pfleiderer, C. Spontaneous skyrmion ground states in magnetic metals. *Nature* **2006**, *442*, 797−801.

(7) Leonov, A. O.; Mostovoy, M. Multiply periodic states and isolated skyrmions in an anisotropic frustrated magnet. *Nat. Commun.* **2015**, *6*, 8275.

(8) Heinze, S.; von Bergmann, K.; Menzel, M.; Brede, J.; Kubetzka, A.; Wiesendanger, R.; Bihlmayer, G.; Blügel, S. Spontaneous atomic-scale magnetic skyrmion lattice in two dimensions. *Nat. Phys.* **2011**, *7*, 713−718.

(9) Ezawa, M. Giant skyrmions stabilized by dipole-dipole interactions in thin ferromagnetic films. *Phys. Rev. Lett.* **2010**, *105*, 197202.

(10) Göbel, B.; Mertig, I.; Tretiakov, O. A. Beyond skyrmions: Review and perspectives of alternative magnetic quasiparticles. *Phys. Rep.* **2021**, *895*, 1.

(11) Hayami, S.; Motome, Y. Topological spin crystals by itinerant frustration. *J. Phys.: Condens. Matter* **2021**, *33*, 443001.

(12) Rohart, S.; Thiaville, A. Skyrmion confinement in ultrathin film nanostructures in the presence of Dzyaloshinskii-Moriya interaction. *Phys. Rev. B* **2013**, *88*, 184422.

(13) Taguchi, Y.; Oohara, Y.; Yoshizawa, H.; Nagaosa, N.; Tokura, Y. Spin chirality, Berry phase, and anomalous Hall effect in a frustrated ferromagnet. *Science* **2001**, *291*, 2573−2576.

(14) Onoda, S.; Nagaosa, N. Spin chirality fluctuations and anomalous Hall effect in itinerant ferromagnets. *Phys. Rev. Lett.* **2003**, *90*, 196602.

(15) Kanazawa, N.; Onose, Y.; Arima, T.; Okuyama, D.; Ohoyama, K.; Wakimoto, S.; Kakurai, K.; Ishiwata, S.; Tokura, Y. Large topological Hall effect in a short-period helimagnet MnGe. *Phys. Rev. Lett.* **2011**, *106*, 156603.

(16) Kalitsov, A.; Canals, B.; Lacroix, C. Anomalous Hall effect due to magnetic chirality in the pyrochlore lattice. *J. Phys.: Conf. Ser.* **2009**, *145*, 012020.

(17) Denisov, K. S.; Rozhansky, I. V.; Averkiev, N. S.; Lähderanta, E. General theory of the topological Hall effect in systems with chiral spin textures. *Phys. Rev. B* **2018**, *98*, 195439.

(18) Bruno, P.; Dugaev, V. K.; Taillefumier, M. Topological Hall effect and Berry phase in magnetic nanostructures. *Phys. Rev. Lett.* **2004**, *93*, 096806.

(19) Chen, Y.; Zhu, Y.; Lin, R.; Niu, W.; Liu, R.; Zhuang, W.; Zhang, X.; Liang, J.; Sun, W.; Chen, Z.; Hu, Y.; Song, F.; Zhou, J.; Wu, D.; Ge, B.; Yang, H.; Zhang, R.; Wang, X. Observation of colossal topological Hall effect in noncoplanar ferromagnet Cr_5Te_6 thin films. *Adv. Funct. Mater.* **2023**, *33*, 2302984.

(20) Zhou, Y.; Li, S.; Liang, X.; Zhou, Y. Topological spin textures: Basic physics and devices. *Adv. Mater.* **2024**, *37*, 2312935.

(21) Zhang, X.; Zhou, Y.; Song, K. M.; Park, T.-E.; Xia, J.; Ezawa, M.; Liu, X.; Zhao, W.; Zhao, G.; Woo, S. Magnetic skyrmion-based artificial synapse for neuromorphic computing. *J. Phys.: Condens. Matter* **2020**, *32*, 143001.

(22) Zhou, Y. Magnetic skyrmions: intriguing physics and new spintronic device concepts. *Natl. Sci. Rev.* **2019**, *6*, 210.

(23) Lindfors-Vrejoiu, I.; Ziese, M. Topological Hall effect in antiferromagnetically coupled $SrRuO_3/La_{0.7}Sr_{0.3}MnO_3$ epitaxial heterostructures. *Phys. Status Solidi B* **2017**, *254*, 1600556.

(24) Matsuno, J.; Ogawa, N.; Yasuda, K.; Kagawa, F.; Koshibae, W.; Nagaosa, N.; Tokura, Y.; Kawasaki, M. Interface-driven topological Hall effect in $SrRuO_3/SrIrO_3$ bilayer. *Sci. Adv.* **2016**, *2*, No. e1600304.

(25) Wang, L.; Feng, Q.; Kim, Y.; Kim, R.; Lee, K. H.; Pollard, S. D.; Shin, Y. J.; Zhou, H.; Peng, W.; Lee, D.; Meng, W.; Yang, H.; Han, J. H.; Kim, M.; Lu, Q.; Noh, T. W. Ferroelectrically tunable magnetic skyrmions in ultrathin oxide heterostructures. *Nat. Mater.* **2018**, *17*, 1087−1094.

(26) Wang, H.; Dai, Y.; Liu, Z.; Xie, Q.; Liu, C.; Lin, W.; Liu, L.; Yang, P.; Wang, J.; Venkatesan, T. V.; Chow, G. M.; Tian, H.; Zhang, Z.; Chen, J. Overcoming the limits of the interfacial Dzyaloshinskii-Moriya interaction by antiferromagnetic order in multiferroic heterostructures. *Adv. Mater.* **2020**, *32*, 1904415.

(27) Seddon, S. D.; Dogaru, D. E.; Holt, S. J. R.; Rusu, D.; Peters, J. J. P.; Sanchez, A. M.; Alexe, M. Real-space observation of ferroelectrically induced magnetic spin crystal in $SrRuO_3$. *Nat. Commun.* **2021**, *12*, 2007.

(28) Wang, W.; Daniels, M. W.; Liao, Z.; Zhao, Y.; Wang, J.; Koster, G.; Rijnders, G.; Chang, C.-Z.; Xiao, D.; Wu, W. Spin chirality fluctuation in two-dimensional ferromagnets with perpendicular magnetic anisotropy. *Nat. Mater.* **2019**, *18*, 1054−1059.

(29) Koster, G.; Klein, L.; Siemons, W.; Rijnders, G.; Dodge, J. S.; Eom, C.-B.; Blank, D. H. A.; Beasley, M. R. Structure, physical properties, and applications of $SrRuO_3$ thin films. *Rev. Mod. Phys.* **2012**, *84*, 253−298.

(30) Klein, L.; Dodge, J. S.; Ahn, C. H.; Snyder, G. J.; Geballe, T. H.; Beasley, M. R.; Kapitulnik, A. Anomalous spin scattering effects in the badly metallic itinerant ferromagnet $SrRuO_3$. *Phys. Rev. Lett.* **1996**, *77*, 2774−2777.

(31) Skoropata, E.; Mazza, A.; Herklotz, A.; Ok, J.; Eres, G.; Brahlek, M.; Charlton, T.; Lee, H.; Ward, T. Post-synthesis control of Berry phase driven magnetotransport in $SrRuO_3$ films. *Phys. Rev. B* **2021**, *103*, 085121.

(32) Tian, Y.; Wang, S.; Wei, X.; Yang, R.; Jin, K. Anomalous Hall effect superimposed in polycrystalline $SrRuO_3$ thick film. *Appl. Phys. Lett.* **2022**, *120*, 142404.

(33) Wang, L.; Feng, Q.; Lee, H. G.; Ko, E. K.; Lu, Q.; Noh, T. W. Controllable thickness inhomogeneity and Berry curvature engineering of anomalous Hall effect in $SrRuO_3$ ultrathin films. *Nano Lett.* **2020**, *20*, 2468.

(34) Kimbell, G.; Sass, P. M.; Woltjes, B.; Ko, E. K.; Noh, T. W.; Wu, W.; Robinson, J. W. A. Two-channel anomalous Hall effect in $SrRuO_3$. *Phys. Rev. Mater.* **2020**, *4*, 054414.

(35) Wysocki, L.; Yang, L.; Gunkel, F.; Dittmann, R.; van Loosdrecht, P. H. M.; Lindfors-Vrejoiu, I. Validity of magnetotransport detection of skyrmions in epitaxial $SrRuO_3$ heterostructures. *Phys. Rev. Mater.* **2020**, *4*, 054402.

(36) Qin, Q.; Liu, L.; Lin, W.; Shu, X.; Xie, Q.; Lim, Z.; Li, C.; He, S.; Chow, G.; Chen, J. Emergence of topological Hall effect in a $SrRuO_3$ single layer. *Adv. Mater.* **2019**, *31*, 1807008.

(37) Kimbell, G.; Kim, C.; Wu, W.; Cuoco, M.; Robinson, J. W. A. Challenges in identifying chiral spin textures via the topological Hall effect. *Commun. Mater.* **2022**, *3*, 19.

(38) Haldane, F. D. M. Model for a quantum Hall effect without Landau levels: Condensed-matter realization of the parity anomaly. *Phys. Rev. Lett.* **1988**, *61*, 2015−2018.

(39) Xiao, D.; Zhu, W. G.; Ran, Y.; Nagaosa, N.; Okamoto, S. Interface engineering of quantum Hall effects in digital transition-metal oxide heterostructures. *Nat. Commun.* **2011**, *2*, 596.

(40) Rüegg, A.; Mitra, C.; Demkov, A. A.; Fiete, G. A. Lattice distortion effects on topological phases in $(LaNiO_3)_2/(LaAlO_3)_N$ heterostructures grown along the [111] direction. *Phys. Rev. B* **2013**, *88*, 115146.

(41) Si, L.; Janson, O.; Li, G.; Zhong, Z.; Liao, Z.; Koster, G.; Held, K. Quantum anomalous Hall state in ferromagnetic $SrRuO_3$ (111) bilayers. *Phys. Rev. Lett.* **2017**, *119*, 026402.

(42) Marthinsen, A.; Griffin, S. M.; Moreau, M.; Grande, T.; Tybell, T.; Selbach, S. M. Goldstone-like phonon modes in a (111)-strained perovskite. *Phys. Rev. Mater.* **2018**, *2*, 014404.

(43) Wang, Z.; Qi, W.; Bi, J.; Li, X.; Chen, Y.; Yang, F.; Cao, Y.; Gu, L.; Zhang, Q.; Wang, H.; Zhang, J.; Guo, J.; Liu, X. Anomalous strain effect in heteroepitaxial $SrRuO_3$ films on (111) $SrTiO_3$ substrates. *Chin. Phys. B* **2022**, *31*, 126801.

(44) Lin, W.; Liu, L.; Liu, Q.; Li, L.; Shu, X.; Li, C.; Xie, Q.; Jiang, P.; Zheng, X.; Guo, R.; Lim, Z.; Zeng, S.; Zhou, G.; Wang, H.; Zhou, J.; Yang, P.; Ariando, A.; Pennycook, S. J.; Xu, X.; Zhong, Z.; Wang, Z.; Chen, J. Electric field control of the magnetic Weyl fermion in an epitaxial $SrRuO_3$ (111) thin film. *Adv. Mater.* **2021**, *33*, 2101316.

(45) Ding, Z.; Chen, X.; Wang, Z.; Zhang, Q.; Yang, F.; Bi, J.; Lin, T.; Wang, Z.; Wu, X.; Gu, M.; Meng, M.; Cao, Y.; Gu, L.; Zhang, J.; Zhong, Z.; Liu, X.; Guo, J. Magnetism and Berry phase manipulation in an emergent structure of perovskite ruthenate by (111) strain engineering. *npj Quantum Mater.* **2023**, *8*, 43.

(46) Rastogi, A.; Brahlek, M.; Ok, J. M.; Liao, Z.; Sohn, C.; Feldman, S.; Lee, H. N. Metal-insulator transition in (111) $SrRuO_3$ ultrathin films. *APL Mater.* **2019**, *7*, 091106.

(47) Tian, D.; Liu, Z.; Shen, S.; Li, Z.; Zhou, Y.; Liu, H.; Chen, H.; Yu, P. Manipulating Berry curvature of $SrRuO_3$ thin films via epitaxial strain. *Proc. Natl. Acad. Sci. U.S.A.* **2021**, *118*, No. e2101946118.

(48) Kan, D.; Moriyama, T.; Kobayashi, K.; Shimakawa, Y. Alternative to the topological interpretation of the transverse resistivity anomalies in $SrRuO_3$. *Phys. Rev. B* **2018**, *98*, 180408.

(49) Wang, W.; Li, L.; Liu, J.; Chen, B.; Ji, Y.; Wang, J.; Cheng, G.; Lu, Y.; Rijnders, G.; Koster, G.; Wu, W.; Liao, Z. Magnetic domain engineering in $SrRuO_3$ thin films. *npj Quantum Mater.* **2020**, *5*, 73.

(50) Jiang, J.; Xiao, D.; Wang, F.; Shin, J.-H.; Andreoli, D.; Zhang, J.; Xiao, R.; Zhao, Y.-F.; Kayyalha, M.; Zhang, L.; Wang, K.; Zang, J.; Liu, C.; Samarth, N.; Chan, M. H. W.; Chang, C.-Z. Concurrence of quantum anomalous Hall and topological Hall effects in magnetic topological insulator sandwich heterostructures. *Nat. Mater.* **2020**, *19*, 732.

(51) Liu, C.; Zang, Y.; Ruan, W.; Gong, Y.; He, K.; Ma, X.; Xue, Q.; Wang, Y. Dimensional crossover-induced topological Hall effect in a magnetic topological insulator. *Phys. Rev. Lett.* **2017**, *119*, 176809.

(52) Zhao, D.; Zhang, L.; Malik, I. A.; Liao, M.; Cui, W.; Cai, X.; Zheng, C.; Li, L.; Hu, X.; Zhang, D.; Zhang, J.; Chen, X.; Jiang, W.; Xue, Q. Observation of unconventional anomalous Hall effect in epitaxial CrTe thin films. *Nano Res.* **2018**, *11*, 3116−3121.

(53) Li, Y.; Kanazawa, N.; Yu, X. Z.; Tsukazaki, A.; Kawasaki, M.; Ichikawa, M.; Jin, X. F.; Kagawa, F.; Tokura, Y. Robust formation of skyrmions and topological Hall effect anomaly in epitaxial thin films of MnSi. *Phys. Rev. Lett.* **2013**, *110*, 117202.

(54) Shao, Q.; Liu, Y.; Yu, G.; Kim, S. K.; Che, X.; Tang, C.; He, Q. L.; Tserkovnyak, Y.; Shi, J.; Wang, K. L. Topological Hall effect at above room temperature in heterostructures composed of a magnetic insulator and a heavy metal. *Nat. Electron.* **2019**, *2*, 182.

(55) Li, X.; Zhou, J.; Shen, L.; Sun, B.; Bai, H.; Wang, W. Exceptionally high saturation magnetic flux density and ultralow coercivity via an amorphous-nanocrystalline transitional microstructure in an FeCo-based alloy. *Adv. Mater.* **2023**, *35*, 2205863.

(56) Sohn, B.; Kim, B.; Park, S. Y.; Choi, H. Y.; Moon, J. Y.; Choi, T.; Choi, Y. J.; Zhou, H.; Choi, J. W.; Bombardi, A.; Porter, D. G.; Chang, S. H.; Han, J. H.; Kim, C. Stable humplike Hall effect and noncoplanar spin textures in $SrRuO_3$ ultrathin films. *Phys. Rev. Research* **2021**, *3*, 023232.

(57) Rusu, D.; Peters, J. J. P.; Hase, T. P. A.; Gott, J. A.; Nisbet, G. A. A.; Strempfer, J.; Haskel, D.; Seddon, S. D.; Beanland, R.; Sanchez, A. M.; Alexe, M. Ferroelectric incommensurate spin crystals. *Nature* **2022**, *602*, 240−244.

(58) Chen, J. P.; Zhang, D. W.; Liu, J. M. Exotic skyrmion crystals in chiral magnets with compass anisotropy. *Sci. Rep.* **2016**, *6*, 29126.

(59) Nagaosa, N.; Tokura, Y. Topological properties and dynamics of magnetic skyrmions. *Nat. Nanotechnol.* **2013**, *8*, 899−911.

(60) Kong, L. Y. Research progress on topological properties and micro-magnetic simulation study in dynamics of magnetic skyrmions. *Acta Phys. Sin.* **2018**, *67*, 137506.

(61) Wang, H.; Dai, Y.; Chow, G.-M.; Chen, J. Topological Hall transport: Materials, mechanisms and potential applications. *Prog. Mater. Sci.* **2022**, *130*, 100971.

(62) Zhang, P.; Das, A.; Barts, E.; Azhar, M.; Si, L.; Held, K.; Mostovoy, M.; Banerjee, T. Robust skyrmion-bubble textures in $SrRuO_3$ thin films stabilized by magnetic anisotropy. *Phys. Rev. Research* **2020**, *2*, 032026.

(63) Kwon, H. Y.; Bu, K. M.; Wu, Y. Z.; Won, C. Effect of anisotropy and dipole interaction on long-range order magnetic structures generated by Dzyaloshinskii−Moriya interaction. *J. Magn. Magn. Mater.* **2012**, *324*, 2171−2176.

(64) Scaramucci, A.; Shinaoka, H.; Mostovoy, M. V.; Müller, M.; Mudry, C.; Troyer, M.; Spaldin, N. A. Multiferroic magnetic spirals induced by random magnetic exchanges. *Phys. Rev. X* **2018**, *8*, 011005.

(65) Ishiwata, S.; Nakajima, T.; Kim, J.-H.; Inosov, D. S.; Kanazawa, N.; White, J. S.; Gavilano, J. L.; Georgii, R.; Seemann, K. M.; Brandl, G.; Manuel, P.; Khalyavin, D. D.; Seki, S.; Tokunaga, Y.; Kinoshita, M.; Long, Y. W.; Kaneko, Y.; Taguchi, Y.; Arima, T.; Keimer, B.; Tokura, Y. Emergent topological spin structures in the centrosymmetric cubic perovskite $SrFeO_3$. *Phys. Rev. B* **2020**, *101*, 134406.

(66) Mostovoy, M. Helicoidal ordering in iron perovskites. *Phys. Rev. Lett.* **2005**, *94*, 137205.

(67) Dahlbom, D.; Zhang, H.; Miles, C.; Quinn, S.; Niraula, A.; Thipe, B.; Wilson, M.; Matin, S.; Mankad, H.; Hahn, S.; Pajerowski, D.; Johnston, S.; Wang, Z.; Lane, H.; Li, Y. W.; Bai, X.; Mourigal, M.; Batista, C. D.; Barros, K.; Sunny, J.: A Julia Package for Spin Dynamics. https://github.com/SunnySuite/Sunny.jl, (accessed August 8, 2024).

(68) Lu, X.; Fei, R.; Zhu, L.; Yang, L. Meron-like topological spin defects in monolayer $CrCl_3$. *Nat. Commun.* **2020**, *11*, 4724.

(69) Cenker, J.; Sivakumar, S.; Xie, K.; Miller, A.; Thijssen, P.; Liu, Z.; Dismukes, A.; Fonseca, J.; Anderson, E.; Zhu, X.; Roy, X.; Xiao, D.; Chu, J.-H.; Cao, T.; Xu, X. Reversible strain-induced magnetic phase transition in a van der Waals magnet. *Nat. Nanotechnol.* **2022**, *17*, 256−261.

(70) Yokota, T. Numerical investigation of magnetic bubble types in a two-dimensional ferromagnetic system with dipole-dipole interactions. *J. Phys. Soc. Jpn.* **2019**, *88*, 084702.